Water Deposition Rates onto Mars' South Polar Massive CO2 Ice Deposit

Peter Benjamin Buhler[1]

[1]Planetary Science Institute

November 24, 2022

Abstract

Mars' polar layered deposits record critical information about its climate history. Here, I numerically model formation of alternating layers of CO2 and H2O ice in Mars' south polar Massive CO2 Ice Deposit to reconstruct its H2O ice depositional history over the past 510 thousand years. Statistical analyses of ˜10^9 model runs favor a best-fit historical H2O ice deposition function that exponentially decreases with obliquity, with ˜1, 0.1, and 0.01 mm yr^-1 rates for 20, 24, and 28 deg. obliquity, respectively. Recovery of a south polar H2O-ice-deposition-versus-obliquity function is novel and important for elucidating Mars' global water cycle; previous south polar layer analyses were limited to calculation of net average deposition rates over millions of years.

Hosted file

essoar.10512516.1.docx available at https://authorea.com/users/553019/articles/604945-water-deposition-rates-onto-mars-south-polar-massive-co2-ice-deposit

Water Deposition Rates onto Mars' South Polar Massive CO$_2$ Ice Deposit

Author: P.B. Buhler[1]

Affiliation: [1]Planetary Science Institute; 1700 East Fort Lowell, Suite 106, Tucson, AZ 85719-2395, USA

Key Points

- I model H$_2$O layer formation in Mars' Massive CO$_2$ Ice Deposit to calculate H$_2$O ice deposition rates over the past 510 thousand years

- The best-fit deposition rate exponentially decreases with obliquity: ~1, 0.1, & 0.01 mm yr^{-1} for 20, 24, & 28° obliquity, respectively

- Recovery of a south polar deposition-versus-obliquity function, rather than ~million-year averaged rates, is novel

Abstract

Mars' polar layered deposits record critical information about its climate history. Here, I numerically model formation of alternating layers of CO$_2$ and H$_2$O ice in Mars' south polar Massive CO$_2$ Ice Deposit to reconstruct its H$_2$O ice depositional history over the past 510 thousand years. Statistical analyses of ~10^9 model runs favor a best-fit historical H$_2$O ice deposition function that exponentially decreases with obliquity, with ~1, 0.1, and 0.01 mm yr^{-1} rates for 20, 24, and 28° obliquity, respectively. Recovery of a south polar H$_2$O-ice-deposition-versus-obliquity function is novel and important for elucidating Mars' global water cycle; previous south polar layer analyses were limited to calculation of net average deposition rates over millions of years.

Plain Language Summary

Mars' south pole hosts a deposit of alternating CO$_2$ and H$_2$O ice layers, which contain a record of global H$_2$O and CO$_2$ transport as Mars' orbit evolved during the past 510 thousand years. I created a numerical model to simulate the build-up of the layers over time and ran the model approximately one billion times, each time using a different governing function of H$_2$O ice deposition as a function of Mars' orbital configuration. Using statistical analysis, I found that that an H$_2$O ice deposition function that exponentially decreases as a function of obliquity (spin-axis tilt) best recreates the observed layer sequence. Recovery of south polar H$_2$O-ice-deposition-versus-obliquity function is novel and important for elucidating Mars' global water cycle. Previous south polar layer analyses were limited to calculation of average net deposition rates over millions of years.

1. Introduction

Mars' polar deposits contain rich records of historical climatic processes (Smith et al. 2020; Becerra et al., 2021). This study focuses on deciphering the record contained in alternating layers of CO$_2$ and H$_2$O ice in Mars' south polar Massive CO$_2$ Ice Deposit (MCID; Phillips et al., 2011; Bierson et al., 2016). The MCID's

mass approximately equals that of Mars' current, principally CO_2 atmosphere (Putzig et al., 2018), reaches up to ~1 km thickness, and contains spatially discontinuous H_2O ice Bounding Layers (BLs) that divide the CO_2 ice into layers (Fig. 1; Bierson et al., 2016). CO_2 layers reach 100s-of-meter maximum thicknesses, while H_2O layers reach 10s-of-meter maximum thicknesses (Alwarda and Smith, 2021).

The MCID formed through exchange between polar CO_2 ice, atmospheric CO_2, and CO_2 adsorbed in regolith (soil), driven by changes in the latitudinal distribution of sunlight due to Mars' cyclic orbital evolution over the past 510 kyr (Fig. 2; Buhler et al., 2020; Buhler and Piqueux, 2021). When obliquity decreases, polar sunlight decreases, and CO_2 ice (along with H_2O ice and dust impurities) accumulates onto the MCID; when obliquity increases, polar sunlight increases, and CO_2 ablates from the MCID. BLs are lag layers of residual refractory material (H_2O ice, dust) left behind when the CO_2 ice ablates. Previous modeling of BL formation has been simplistic (Buhler et al., 2020).

Here, I introduce a numerical model of lag production to calculate historical rates of H_2O ice deposition onto the MCID. The main goal is to use the model to determine a best-fit functional form, and associated parameters, for H_2O ice deposition rate r_{H_2O} as a function of orbital parameters that yields a predicted stratigraphic column most closely matching the observed MCID stratigraphy.

2. Methods

2.1 MCID Stratigraphic Model

The flux of CO_2 ice and r_{H_2O} are calculated in 1-kyr timesteps. CO_2 ice flux includes exchange between the MCID, atmosphere, and regolith, which depends on latitudinal insolation as a function of obliquity (implemented exactly as in Buhler and Piqueux (2021), using parameters listed in their appendix). The model uses regolith properties: thickness = 250 m, albedo = 0.2, specific surface area = $4 \times 10^4 \ m^2 kg^{-1}$, and thermal conductivity = $0.5 \ Wm^{-1}K^{-1}$; sensitivity tests across the Buhler and Piqueux (2021) 3-σ solution range for these parameters yield «1-σ differences in predicted r_{H_2O}. r_{H_2O} depends on a functional form relating r_{H_2O} to various orbital parameters (§2.2; Table 1). The model outputs a 1-kyr-resolution time-marching MCID stratigraphic column (Fig. 2A). Although r_{H_2O} and BL composition are discussed as pure H_2O ice, they almost certainly include a dust component.

2.1.1 Periods of CO_2 Ice Accumulation

At each timestep while CO_2 is accumulating, CO_2 ice deposition is calculated as in Buhler and Piqueux (2021). H_2O ice deposits as an intimate mixture with thickness specified by an r_{H_2O} function (§2.2, Table 1). A new layer is added to the column top with appropriate fractional H_2O content and thickness equal to the sum of the deposited CO_2 and H_2O ice layer thicknesses (Fig. 2A).

2.1.2 Periods of CO_2 Ice Ablation

At each timestep while CO_2 is ablating, CO_2 ice ablation is calculated as in Buhler and Piqueux (2021). A pure H_2O ice layer grows at the top of the column at a rate equal to the sum of 'liberated' and 'deposited' H_2O ice thicknesses, as described below.

'Liberated' H_2O ice is the summation of H_2O ice in the (completely and/or partially) ablated CO_2 layer(s). Conceptually, 'liberated' H_2O ice sources at the bottom of a growing BL as CO_2 sublimes beneath the BL. If CO_2 ice between two BLs completely ablates, they merge (Fig. 2A).

'Deposited' H_2O ice accumulates at the column top according to an r_{H_2O} function (§2.2, Table 1). Conceptually, 'deposited' H_2O sources from the atmosphere onto a thin perennial CO_2 deposit overlying the topmost BL, i.e., a "paleo-" South Polar Residual Cap (SPRC; e.g., Kieffer, 1979; Malin et al., 2001) that likely exists whenever the MCID is ablating (Buhler et al., 2020). H_2O ice within the paleo-SPRC sifts down to the topmost BL as the paleo-SPRC regionally accumulates and ablates (Thomas et al., 2016; Buhler et al., 2017). SPRC recycling timescales are ~100 years (Byrne and Ingersoll, 2003; Thomas et al., 2005, 2016), shorter than the model timestep, so this full process is not explicitly modeled but rather treated as direct H_2O ice deposition onto the column top.

2.2 Statistical Determination of Best-Fit H_2O Deposition Rate

Various r_{H_2O} polynomial and exponential formulations as a function of obliquity, eccentricity, longitude of perihelion, or south polar insolation were considered (Table 1). All models have equal prior probability, and all parameters have uniform prior probability. 10^8 iterations of each model r_{H_2O} formulation were run through a Buhler and Piqueux (2021) Markov Chain Monte Carlo (MCMC) routine. Relative likelihoods H of each model were assessed using Bayes factors B, which reward better fits but penalize higher complexity (e.g., Kass and Raftery, 1995):

(Eq. 1) $B_{i,j} = \frac{\text{pr}(\mathbf{D}|H_i)}{\text{pr}(\mathbf{D}|H_j)}$

Model likelihood $\text{pr}(\mathbf{D}|H)$ is the average of likelihoods sampled at each MCMC m-indexed step (Kass and Raftery, 1995):

(Eq. 2) $\text{pr}(\mathbf{D}|H_i) = \frac{1}{M} \sum_{m=1}^{M} \prod_{d=1}^{D} \frac{1}{\sqrt{2\pi\sigma_d^2}} \exp\left(-\frac{1}{2}\left(\frac{(z(_{\mathbf{i},\mathbf{m}})-\mu_d)^2}{\sigma_d^2}\right)\right)$

The righthand side of the equation is the product of the likelihoods for the mean μ and standard deviation σ of each d-indexed datapoint of BL thickness and model-predicted thickness z from model parameters , assuming a Gaussian variance, as is appropriate to the data at hand.

2.3 Nomenclature

Alwarda and Smith (2021) discovered a lenticular deposit of CO_2 embedded within one of the BLs (Fig. 1B), prompting new nomenclature. I adopt their CO_2 layer names but modify their BL names. Alwarda and Smith (2021) refer

to the lens region (blue outline, Fig. 1A) lower BL member as "BL2", upper BL member as "BL3", and surrounding BL as merged "BL2+3" (black outline, Fig. 1A). They referred to western BLs (white outlines, Fig. 1A) as "BL2." However, western BLs are here referred to as "BL2+3" because modeling (Fig. 2; Buhler et al., 2020) indicates that western BLs are merged material corresponding to lens-region BL2 and BL3 deposition, rather than BL2 alone.

2.4 Comparison to Observed Stratigraphy

Models were fit to observations from two regions (Fig. 1A; Alwarda and Smith, 2021). Region 1 is near [86° S, 270° E], clipped to where BL2+3 overlies BL1 (Fig. 1C-D); here, observed BL1 thickness is 31 ± 5 m and BL2+3 thickness is 30 ± 5 m. Region 2 is near [86° S, 315° E], clipped to where BL3 is separably observed to overlie BL2; here, observed BL2 thickness is 34 ± 8 m and BL3 thickness is 37 ± 7 m. Quoted uncertainty is the quadratic addition of the 10-m vertical Shallow Radar (SHARAD) instrument resolution (Seu et al., 2007; Foss et al., 2017; divided by $\sqrt{N}$, for $N = 4436$ and 909 observations in Region 1 and 2, respectively) and BL lateral thickness variation.

Models were constrained by the SHARAD non-observation of BL4 by placing an equal probability prior for BL4 10 m (SHARAD's resolving power) and a Gaussian decrease in prior probability with a 1-σ scale of 5 m (half of SHARAD resolving power) for BL4 > 10 m; an equivalent statement of this constraint is that BL4 has a 50%, 68%, 95%, or 99% likelihood of being resolved if it were 10, 15, 20, or 25 m thick, respectively. Finally, Region 2 modeling assumes H_2O ice within the 60 meters of CO_2 directly above BL2 remains trapped within the CO_2 ice (i.e., the average AA_{3c} lens thickness (Alwarda and Smith, 2021)).

3. Results

Table 1 shows model Bayes factor B, relative to a constant deposition model. A standard interpretation of B is 1-to-3: "marginal", 3-to-20: "positive", 20-to-150: "strong", and >150: "very strong" (Kass and Raftery, 1995). In Region 1, models with r_{H_2O} quadratic dependency on obliquity ε ($B = 65$), eccentricity e ($B = 29$), or peak annual south polar insolation I ($B = 64$) or exponential dependency on ε ($B = 64$) or e ($B = 66$) are "strongly" favored over a constant deposition model. Higher order polynomial models offer only marginally improvement (B «3×), so they are disfavored. In Region 2, the model with exponentially decreasing r_{H_2O}-versus-ε is "strongly" ($B = 21$) favored over a constant r_{H_2O} model; all other models have only marginal improvement (i.e., $B < 3$; Table 1).

B alone does not distinguish between the "strongly" favored models in Region 1. However, the similarity of the model solutions with exponentially decreasing r_{H_2O}-versus-ε in both Region 1 (Fig. 3A) and Region 2 (Fig. 3B) indicate preferring this solution, which is borne out by additional analysis (§4.1-4.2). The favored Region 1 $r_{H_2O} = exp(-0.6923 \times \varepsilon + 13.73)$ and Region 2 $r_{H_2O} = exp(-0.5034 \times \varepsilon + 10.31)$ (Fig. 3A-B).

4

The favored Region 1 r_{H_2O} history (Fig. 2C) and resultant model stratigraphy (Fig. 2A) predict BL1 thickness = $30.4^{+7.3}_{-6.6}$, BL2+3 thickness = $28.3^{+7.3}_{-7.8}$, BL4 thickness = $6.3^{+2.4}_{-2.3}$ m and modern day ($\varepsilon = 25.2°$) $r_{H_2O} = 0.03^{+0.03}_{-0.02}$ mm yr^{-1} (68% confidence intervals). The favored Region 2 model predicts a generally similar (but higher at high ε and lower at low ε) r_{H_2O}-versus-ε relation (Fig. 2C, 3B), BL2 thickness = $33.8^{+7.0}_{-7.8}$, BL3 thickness = $25.6^{+5.0}_{-5.1}$, BL4 thickness = $17.2^{+3.1}_{-3.0}$ m and modern day $r_{H_2O} = 0.09^{+0.02}_{-0.03}$ mm yr^{-1}.

4. Discussion

4.1 Model Performance Interpretation and Assessment

Model r_{H_2O} preference behavior can be understood within the following framework. In Region 1, BL1 and BL2+3 thicknesses are similar, but BL2+3 formed over 2.4× as much time (387-to-94 kyr) as BL1 (510-to-387 kyr; Fig. 2). Likewise, in Region 2, BL2 and BL3 thicknesses are similar, but BL3 formed over 1.7× as much time (238-to-94 kyr) as BL2 (362-to-278 kyr). Thus, favored models yield ~2.4 × higher r_{H_2O} during BL1 formation than during BL2+3 formation in Region 1 and ~1.7 × higher r_{H_2O} during BL2 formation than during BL3 formation in Region 2.

For example, ε variation amplitudes during BL1 formation were higher than during BL2 formation yet oscillated around a ~24° center during both periods (Fig. 2B). Thus, Region 1 r_{H_2O}-versus-ε models degenerately prefer high r_{H_2O} at low ε (Fig. 3A), high ε (Fig. 3D) or both (with minimum r_{H_2O} centered at $\varepsilon \sim 24°$; Fig. 3C) because these solutions yield higher r_{H_2O} during BL1 formation than during BL2+3 formation. All favored solutions tend to maximize r_{H_2O} in the range of orbital parameter space highly represented during BL1 formation as compared to BL2 formation, as can be seen by comparing Fig. 3 solutions vis-à-vis Fig. 2 orbital history.

The constraint from the SHARAD non-observation of BL4 leads to a noticeable underprediction of mean Region 2 BL3 thickness (by 11 m ≈ 30%). However, the z-test statistic $Z = \frac{\mu_{BL3} - X_{BL3}}{\sqrt{\sigma_o^2 + \sigma_m^2}}$ difference between observed μ_{BL3} and model-predicted X_{BL3} BL3 thickness with observed σ_o and modeled σ_m standard deviations is only 1.3 (one-sided p-value = 0.097 > 0.05), providing confidence that the model reasonably represents reality. Other model-predicted BL thicknesses are even closer to observed thicknesses.

The similarity of the favored model solutions in Regions 1 and 2 can be formally assessed using z-testing. The model-predicted sum of Region 2 BL2 and BL3 thickness is $59.4^{+8.6}_{-9.3}$ m, which is larger than Region 1 BL2+3 thickness = $28.3^{+7.3}_{-7.8}$ m with $Z = 2.63$ (one-sided p-value = 0.0043 « 0.05). Given that the Region 2 model both underpredicts BL3 thickness and does not include H_2O ice remaining within the CO_2 ice in the AA_{3c} lens unit, there is significant evidence that r_{H_2O} is larger in Region 2 from $\varepsilon = 20.1 - 26.7°$ (the range sampled by BL records in both regions). Notably, CO_2 ice is only observed in a lens between

BL2 and BL3 in Region 2 (Unit AA_{3c}; Fig. 1A); elsewhere BL2 and BL3 are merged (Alwarda and Smith, 2021), suggesting that regionally high r_{H_2O} may create thick BLs able to locally protect underlying CO_2 ice from subliming (Bierson et al., 2016), even if BLs do not generally protect the MCID from subliming (Buhler et al., 2020).

4.2 Support for Favored Model Selection

4.2.1 Previous Climate Model Predictions for $r_{H_2O} - versus - \varepsilon$

Physics-based climate modeling indicates that r_{H_2O} should decrease as ε increases, given the present distribution of major water ice deposits (e.g., Toon et al., 1980; Jakosky et al., 1993, 1995; Richardson and Wilson, 2002; Mischna et al., 2003; Emmet et al., 2020). Moreover, r_{H_2O} predicted by these models is quantitatively commensurate (within a factor of ~2×) with the model-predicted r_{H_2O} in this present study. Thus, I favor the exponentially decreasing r_{H_2O}-versus-ε model (Fig. 3A) over the quadratic (Fig. 3C) and exponentially increasing (Fig. 3D) models.

One caveat is that Emmett et al. (2020) find that south polar dust deposition rate r_{dust} increases with increasing ε. Specifically, they find, for $\varepsilon = 15$, 20, and 25°: $r_{dust} = $ ~0.005 mm yr^{-1}; for $\varepsilon = 30$°: $r_{dust} = $ ~0.02 mm yr^{-1}, and for $\varepsilon = 35$°: $r_{dust} = $ ~0.3 mm yr^{-1}. Thus, high-ε dust deposition could contribute to the BL formation, potentially supporting a quadratic-ε model with dominant low-ε r_{H_2O} and high-ε r_{dust}. However, the quadratic-ε model (Fig. 3C) indicates significantly larger high-ε deposition rates than Emmet et al. (2020) find, disfavoring this hypothesis.

It is important to note that climate models indicate r_{H_2O} is sensitive to the global water ice reservoir distribution. Specifically, models with large equatorial or mid-latitude ice supplies predict ~constant r_{H_2O} as a function of ε between $\varepsilon = $ ~15-30° (e.g., Levrard et al., 2004; Montmessin et al., 2004; Emmett et al., 2020; Vos et al., 2022). However, those conditions are more applicable to Mars ~5-10 Myr ago, following Mars' most recent prolonged high-obliquity epoch, rather than to the recent (~510 kyr) record preserved in the BLs (e.g., Levrard et al., 2004, 2007; Laskar et al., 2004), and so are not relevant to the model selection at hand.

4.2.2 Previous Climate Model Predictions for r_{H_2O} versus Other Orbital Parameters

Climate models indicate that r_{H_2O} near $\varepsilon = $ ~15-30° is sensitive to longitude of perihelion L_P (e.g., Montmessin et al., 2007; Madeleine et al., 2009; Vos et al., 2019, 2022) due to extra retention of water vapor in the hemisphere closest to the Sun during summer (i.e., the "Clancy effect"; Clancy et al. (1996)). However, polynomial-L_P models only marginally outperform the constant deposition model (Table 1) because L_P completely circulates on shorter (51 kyr) timescales than BL formation (Fig. 2E; Laskar et al., 2004), averaging out any r_{H_2O} variation. Therefore, this study finds neither meaningful r_{H_2O}-versus-L_P

dependency nor rules out such dependency. Notably, the recovery of a robust r_{H_2O}-versus-ε signal (Fig. 3A) indicates that any potential r_{H_2O}-versus-L_P variations are not large enough to obscure the r_{H_2O}-versus-ε relation.

The inflection points in the "strongly favored" r_{H_2O}-versus-e (Fig. 3E) and r_{H_2O}-versus-I (Fig. 3G) quadratic models (at $e = 0.10$ and $I = 240$ W m^{-2}) and the three-orders-of-magnitude r_{H_2O} decrease between $e = 0.6$ and 0.9 in the exponential-e model (Fig. 3H) have neither obvious physical meaning nor correlate with behavior found in prior studies. Therefore, these models are also disfavored.

4.3 Comparison to Previously Found Deposition Rates

4.3.1 Long-term H_2O Deposition Rates

The present work provides insight into Mars' south polar r_{H_2O} over the past ~510 kyr, a different record than targeted by previous quantitative analysis. Previous polar layer analyses include: (1) South Polar Layered Deposit (PLD) records (Becerra et al., 2019), which likely reflect a climate from 10s of Myr ago (Herkenhoff & Plaut, 2000; Koutnik et al., 2002); the Burroughs crater record (72.3°S, 116.6°E; Sori et al., 2022) reflects deposition over ~4.5 Myr in a different environment, both spatially distant and lacking a perennial CO_2 cold trap; (3) North PLD records (e.g., Hvidberg et al., 2012; Becerra et al., 2017) from the past ~1 Myr.

H_2O-ice-plus-dust deposition rates calculated from the SPLD, Burroughs crater, and NPLD records are 0.13–0.39 mm yr^{-1}, 0.13 mm yr^{-1}, and 0.55 mm yr^{-1}, respectively. Applying the best-fit r_{H_2O} from the present study extrapolated (using §3 best-fit equations) to the ε history over the past 1 Myr and 4.5 Myr (Laskar et al., 2004) yields an average rate $0.92^{+0.23}_{-0.25}$ and $0.79^{+0.21}_{-0.20}$ mm yr^{-1}, respectively, for Region 1, and $0.79^{+0.18}_{-0.18}$ and $0.71^{+0.16}_{-0.16}$ mm yr^{-1}, respectively, for Region 2. The higher rates found in this study are expected because of the likely lack of ablation in the BL record (Buhler et al., 2020; Innanen et al., 2022) and enhanced deposition due to CO_2 cold trapping (e.g., Richardson and Wilson, 2002).

The calculation of south polar r_{H_2O} as a function of ε presented here is novel compared to previous south polar studies, which obtained average net rates over millions-of-year timescales. Moreover, the calculated rates are derived only for accumulation, isolating the calculation from degeneracies due to ablation.

4.3.2 Present-Day H_2O Deposition

The best-fit solutions for Region 1 and Region 2 predict present-day ($\varepsilon = 25.2°$) $r_{H_2O} = 0.03^{+0.03}_{-0.02}$ mm yr^{-1} and $0.09^{+0.02}_{-0.03}$ mm yr^{-1}, respectively, consistent with previous work. Brown et al. (2014) obtain present-day $r_{H_2O} = 6 \times 10^{12}$ to 1.2×10^{14}g yr^{-1} rates from spectral observations. Extrapolating the deposition rates from Regions 1 and 2 over a cap area of 2×10^{11} m^2 (as done in Brown et al., 2014) for comparison yields $r_{H_2O} = 4.5^{+6.0}_{-4.0} \times 10^{12}$g y$r^{-1}$ and $1.7^{+0.3}_{-0.6} \times$

10^{13}g yr, respectively. Thus, the Region 2 best-fit solution for present-day r_{H_2O} is commensurate with their estimate and the Region 1 r_{H_2O} 68% confidence interval overlaps their low estimate.

Climate modeling by Langevin et al. (2007) predicts present-day r_{H_2O} between several $\times$ 0.1 $-$ to $-$ 1 micron per sol between solar longitudes 189 and 270° (their figure 28), equivalent to a few $\times$ 0.01 $-$ to - 0.1 mm yr^{-1}, or a few $\times 10^{12} - 2 \times 10^{13}$g y$r^{-1}$ (calculated as above), consistent with r_{H_2O} for both Region 1 and 2. Notably, their model and modeling by Pottier et al. (2017) and Montmessin et al. (2004, 2007) predicts spatially inhomogeneous south polar H_2O deposition (although the exact deposition distributions differ between models), consistent with the derivation of different r_{H_2O} in Regions 1 and 2. Spectral observations by Langevin et al. (2007) (their figure 18) also show that H_2O ice band strength varies regionally, but with insufficient spatiotemporal coverage to draw specific conclusions about the depositional pattern.

4.4 Future Study

Model-predicted H_2O fractions within the CO_2 ice are typically of order 1% (Fig. 2A), below current instrumental detection capability (e.g., Lalich et al., 2019). The model results presented here provide quantitative guidance for future instrumentation intended for MCID observation. Additionally, future BL4 thickness measurements would enable testing of the r_{H_2O} function calculated in this study and expand calculation of r_{H_2O} over the entirety of the known BL regions (Fig. 1A) by providing a second stratigraphic tie-point.

Finally, the model presented here can be expanded to include additional processes; for example, to explore the stratigraphic effects of CO_2 glacial flow (Smith et al., 2022). The model can also be used to study lag production in other major planetary ice deposits, potentially including the dark layer underlying the topmost layer of N_2 ice deposits in Sputnik Planitia on Pluto (e.g., White et al., 2017).

5. Conclusion

A new model for the development of H_2O ice bounding layers (BLs) within Mars' Massive CO_2 Ice Deposit (MCID) has been developed and used to quantify the deposition rate of H_2O ice r_{H_2O} onto the MCID over the past 510 kyr in two regions. Markov Chain Monte Carlo (MCMC) analyses of ~10^9 model runs yield a best-fit historical r_{H_2O} that exponentially decreases with obliquity, with ~1, 0.1, and 0.01 mm yr^{-1} rates at 20, 24, and 28° obliquity, respectively, and strongly indicates spatially inhomogeneous r_{H_2O} at the two study regions (up to a factor of ~2-3×, depending on ε). Model-predicted rates for present-day r_{H_2O} are $0.03^{+0.03}_{-0.02}$ mm yr^{-1} at Region 1 [86° S, 270° E] and $0.09^{+0.02}_{-0.03}$ mm yr^{-1} at Region 2 [86° S, 315° E], in agreement with previous studies. The model's ability to recover south polar r_{H_2O} as a function of ε is a novel development; previous studies obtained average net rates over millions-of-year timescales.

Table 1. Bayes factor for all models, as a function of obliquity ε, eccentricity

e, longitude of perihelion L_P, and peak annual south polar insolation I. Bayes factors for favored models are bolded.

Functional form (x indicates ε, e, L_P, or I, respectively)	ε	e	L_P	I
Region 1 Constant: $r_{H_2O} = A_0$	1	1	1	1
Region 1 Linear: $r_{H_2O} = A_1 + B_1 x$	6	0.9	0.6	4
Region 1 Quadratic: $r_{H_2O} = A_2 + B_2 x + C_2 x^2$	**65**	**29**	0.9	**64**
Region 1 Cubic: $r_{H_2O} = A_3 + B_3 x + C_3 x^2 + D_3 x^3$	78	57	0.9	59
Region 1 Quartic: $r_{H_2O} = A_4 + B_4 x + C_4 x^2 + D_4 x^3 + E_4 x^4$	71	72	0.9	55
Region 1 Exponential (dec.): $r_{H_2O} = A_5 \times exp(B_5 x)$	**64**	**66**	6	0.3
Region 1 Exponential (inc.): $r_{H_2O} = A_6 \times exp(B_6 x)$	**63**	0.5	6	4
Region 2 Constant: $r_{H_2O} = A_0$	1	1	1	1
Region 2 Linear: $r_{H_2O} = A_1 + B_1 x$	1.2	1.0	1.1	1.0
Region 2 Quadratic: $r_{H_2O} = A_2 + B_2 x + C_2 x^2$	2.6	1.5	1.0	1.5
Region 2 Cubic: $r_{H_2O} = A_3 + B_3 x + C_3 x^2 + D_3 x^3$	1.5	1.6	1.0	2.2
Region 2 Quartic: $r_{H_2O} = A_4 + B_4 x + C_4 x^2 + D_4 x^3 + E_4 x^4$	2.7	1.2	0.9	2.3
Region 2 Exponential (dec.): $r_{H_2O} = A_5 \times exp(B_5 x)$	**21**	0.5	1.9	1.7
Region 2 Exponential (inc.): $r_{H_2O} = A_6 \times exp(B_6 x)$	<0.1	0.7	<0.1	0.9

Figure 1

B

H₂O
CO₂
AA₂

AA₃d
BL2+3
BL3
BL4
BL2+3
AA₃c
BL2
AA₃b
BL1
AA₃a

C **D** **E**

10

F
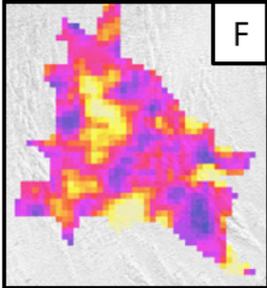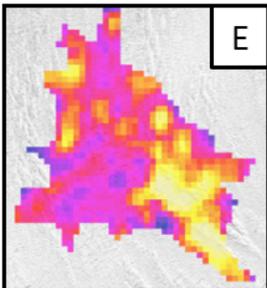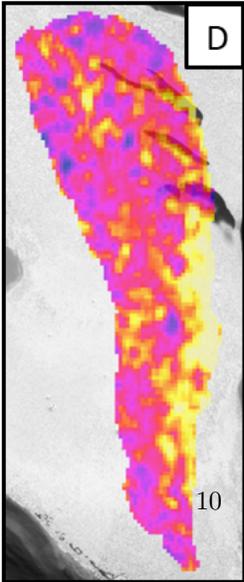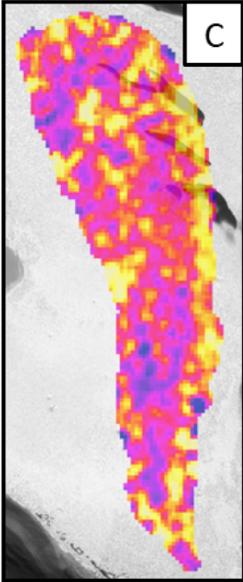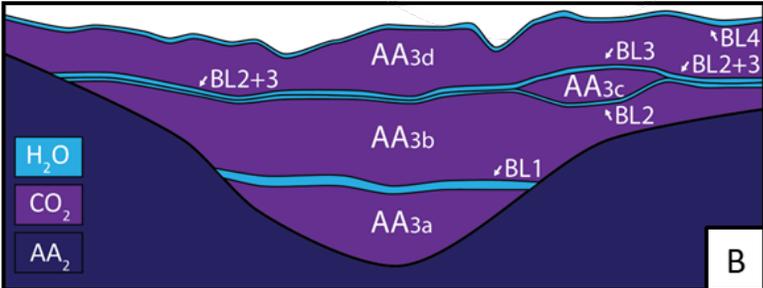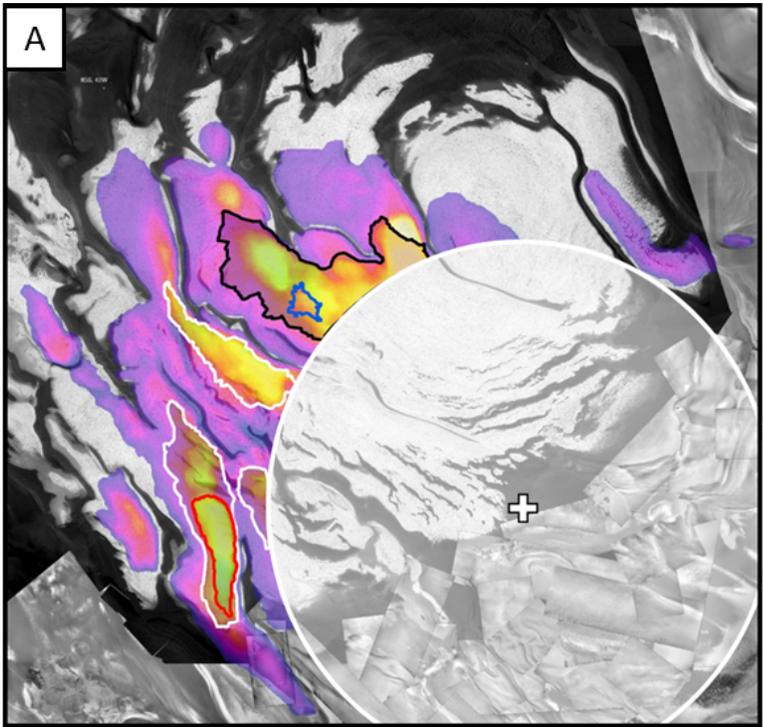
Fig. 1. A. Massive CO_2 Ice Deposit overview. Cross indicates pole. White circle indicates 87° S, within which no RADAR observations are available. 0° E is up, 90° E is right, 180° E is down, and 270° E is left. Colorized region indicates thickness of MCID (Alwarda and Smith, 2021), with outlines of BL units: blue (Region 2 "lens") = "BL3" overlying "BL2", black = "BL2+3", white = "BL2+3" (see §2.3), red (Region 1) = "BL1". Background: THEMIS mosaic (Edwards et al., 2011) and CTX mosaic (Thomas et al., 2016). **B.** Schematic MCID cross section. AA_2 is a basement of dusty H_2O ice. **C.** Thickness of BL1 and **D.** BL2+3 in Region 1, and **E.** BL2 and **F.** BL3 in Region 2 (Alwarda and Smith, 2021). Color range is histogram equalized: cool colors are low and warm are high, for ranges: A. 0-946m, C. 6-50m, D. 16-55m, E. 14-71m, F. 23-69m.

Figure 2
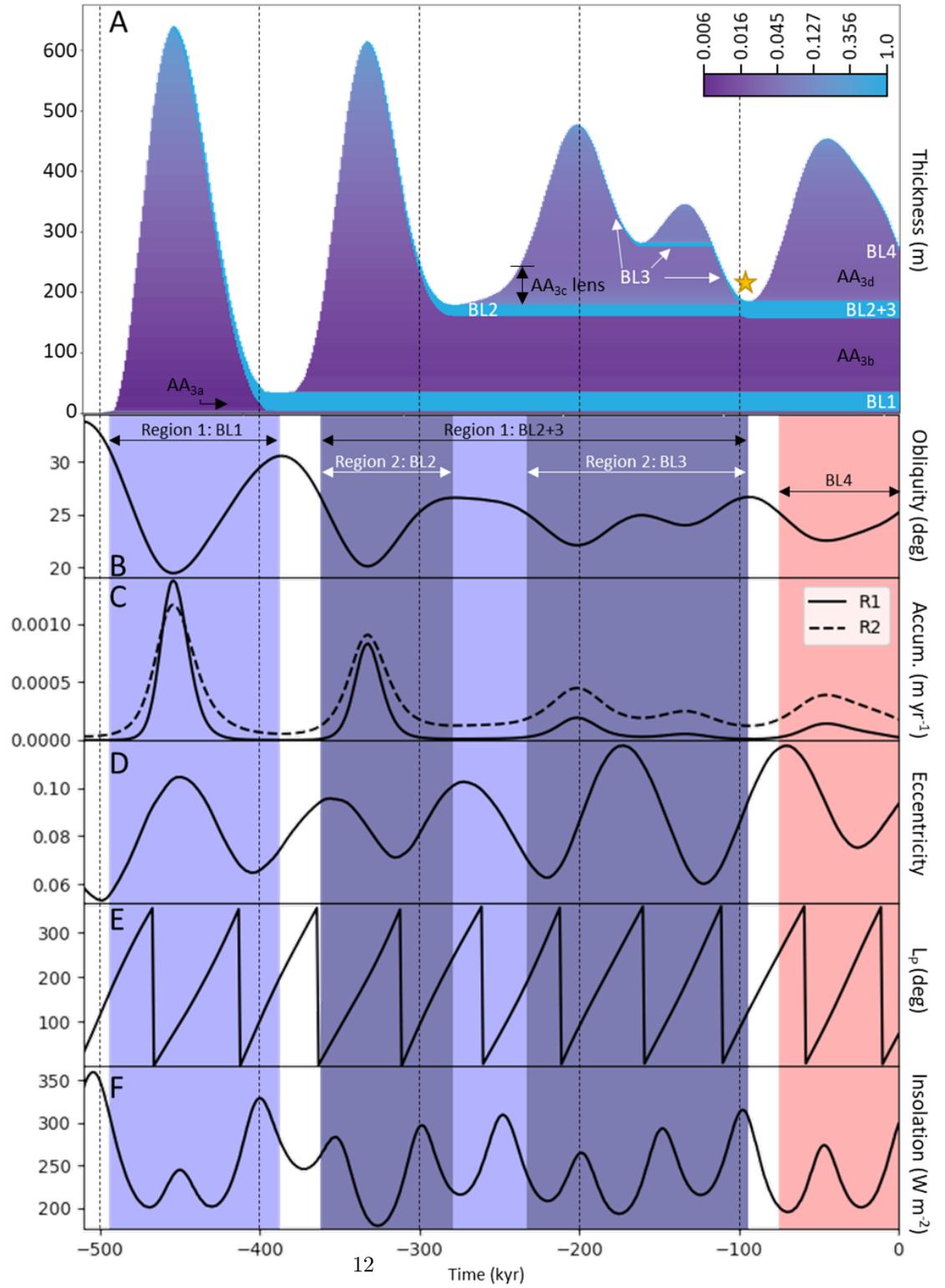
Fig. 2. A. Model stratigraphy for Region 1 favored model. Color indicates fractional H_2O component (log-normalized color bar). Star indicates BL2-BL3 merger. Nb. BL2 and BL3 are constrained not to merge in the Region 2 model (not shown except for AA_{3c} label). **B.** Obliquity, **C.** favored model r_{H_2O} for Regions 1 (solid) and 2 (dashed), **D.** eccentricity, **E.** longitude of perihelion, **F.** peak annual 90° S insolation (B and D-F from Laskar et al., 2004). Blue, dark blue, and red shaded regions indicate deposition of material incorporated into BL1 and BL2+3 in Region 1, BL2 and BL3 in Region 2, and BL4, respectively.

Figure 3
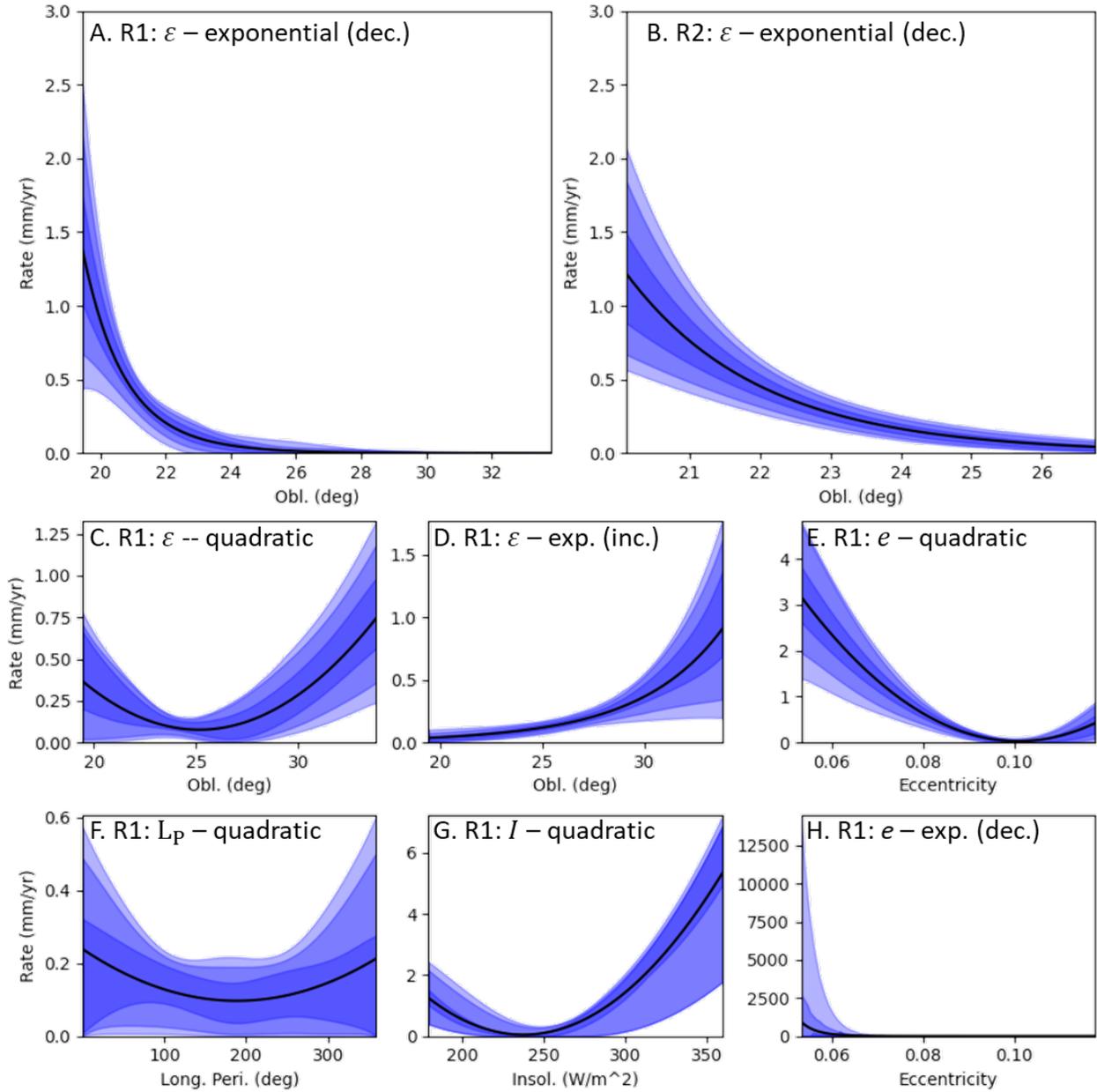
Fig. 3. Model solutions for water ice deposition r_{H_2O} onto the MCID, with best fit (black), and 68% (dark blue), 95% (intermediate blue), and 99% (light blue) confidence intervals, for the range of orbital parameters sampled during BL formation (Figs. 2B, 2D-F). **A.** Favored Region 1 model, **B.** favored Region 2 model (both decreasing exponentials as a function of ε), and **C.** alternate Region 1 model (quadratic function of ε). Examples of other, disfavored models

for Region 1: **D.** increasing exponential as a function of ε, quadratic functions of **E.** eccentricity, **F.** longitude of perihelion, **G.** peak annual south polar insolation, and **H.** decreasing exponential as a function of eccentricity.

Acknowledgements and Data Availability

References

Alwarda, R. and Smith, I.B., 2021. Stratigraphy and volumes of the units within the massive carbon dioxide ice deposits of Mars. *Journal of Geophysical Research: Planets*, *126*(5), p.e2020JE006767.

Becerra, P., Sori, M.M. and Byrne, S., 2017. Signals of astronomical climate forcing in the exposure topography of the North Polar Layered Deposits of Mars. Geophysical Research Letters, 44(1), pp.62-70.

Becerra, P., Sori, M.M., Thomas, N., Pommerol, A., Simioni, E., Sutton, S.S., Tulyakov, S. and Cremonese, G., 2019. Timescales of the climate record in the south polar ice cap of Mars. *Geophysical Research Letters*, *46*(13), pp.7268-7277.

Becerra, P., Smith, I.B., Hibbard, S., Andres, C., Bapst, J., Bramson, A.M., Buhler, P.B., Coronato, A., Diniega, S., Emmett, J. and Galofre, A.G., 2021. Past, Present, and Future of Mars Polar Science: Outcomes and Outlook from the 7th International Conference on Mars Polar Science and Exploration. *The Planetary Science Journal*, *2*(5), p.209.

Bierson, C.J., Phillips, R.J., Smith, I.B., Wood, S.E., Putzig, N.E., Nunes, D. and Byrne, S., 2016. Stratigraphy and evolution of the buried CO2 deposit in the Martian south polar cap. *Geophysical Research Letters*, *43*(9), pp.4172-4179.

Brown, A.J., Piqueux, S. and Titus, T.N., 2014. Interannual observations and quantification of summertime H2O ice deposition on the Martian CO2 ice south polar cap. *Earth and Planetary Science Letters*, *406*, pp.102-109.

Buhler, P.B., Ingersoll, A.P., Ehlmann, B.L., Fassett, C.I. and Head, J.W., 2017. How the martian residual south polar cap develops quasi-circular and heart-shaped pits, troughs, and moats. *Icarus*, *286*, pp.69-93.

Buhler, P.B., Ingersoll, A.P., Piqueux, S., Ehlmann, B.L. and Hayne, P.O., 2020. Coevolution of Mars's atmosphere and massive south polar CO2 ice deposit. *Nature Astronomy*, *4*(4), pp.364-371.

Buhler, P.B. and Piqueux, S., 2021. Obliquity-Driven CO2 Exchange Between Mars' Atmosphere, Regolith, and Polar Cap. *Journal of Geophysical Research: Planets*, *126*(5), p.e2020JE006759.

Buhler, P.B. (2022). Data Tables for Water Deposition Rates onto Mars' South Polar Massive CO2 Ice Deposit (Buhler). figshare. Dataset. https://doi.org/10.6084/m9.figshare.21201199.v1

Byrne, S. and Ingersoll, A.P., 2003. Martian climatic events on timescales of centuries: Evidence from feature morphology in the residual south polar ice cap. *Geophysical research letters*, *30*(13).

Clancy, R.T., Grossman, A.W., Wolff, M.J., James, P.B., Rudy, D.J., Billawala, Y.N., Sandor, B.J., Lee, S.W., Muhleman, D.O., 1996. Water vapor saturation at low altitudes around Mars aphelion: A key to Mars climate? Icarus 122, 36–62

Edwards, C. S., K. J. Nowicki, P. R. Christensen, J. Hill, N. Gorelick, and K. Murray (2011), Mosaicking of global planetary image datasets: 1. Techniques and data processing for Thermal Emission Imaging System (THEMIS) multi-spectral data, J. Geophys. Res., 116, E10008, doi:10.1029/2010JE003755. http://dx.doi.org/10.1029/2010JE003755

Emmett, J.A., Murphy, J.R. and Kahre, M.A., 2020. Obliquity dependence of the formation of the martian polar layered deposits. *Planetary and Space Science*, *193*, p.105047.

Foss, F. J., Putzig, N. E., Campbell, B. A., & Phillips, R. J. (2017). 3D imaging of Mars' polar ice caps using orbital radar data. The Leading Edge, 36(1), 43–57. https://doi.org/10.1190/tle36010043.1

Herkenhoff, K.E. and Plaut, J.J., 2000. Surface ages and resurfacing rates of the polar layered deposits on Mars. *Icarus*, *144*(2), pp.243-253.

Hvidberg, C. S., Fishbaugh, K. E., Winstrup, M., Svensson, A., Byrne, S., & Herkenhoff, K. E. (2012). Reading the climate record of the Martian polar layered deposits. Icarus, 221(1), 405–419. https://doi.org/10.1016/j.icarus.2012.08.009

Innanen, A.C., Landis, M.E., Hayne, P.O. and Moores, J.E., 2022. Possible Atmospheric Water Vapor Contribution from Martian Swiss Cheese Terrain. *LPSC 53, #1969*

Jakosky, B., M. Henderson, and B. G. Mellon, The Mars water cycle at other epochs—Recent history of the polar caps and layered terrain, Icarus, 102, 286 – 297, 1993.

Jakosky, B. M., B. G. Henderson, and M. T. Mellon, Chaotic obliquity and the nature of the Martian climate, J. Geophys. Res., 100, 1579 – 1584, 1995.

Kass, R.E. and Raftery, A.E., 1995. Bayes factors. *Journal of the american statistical association*, *90*(430), pp.773-795.

Kieffer, H.H., 1979. Mars south polar spring and summer temperatures: A residual CO2 frost. *Journal of Geophysical Research: Solid Earth*, *84*(B14), pp.8263-8288.

Koutnik, M., Byrne, S. and Murray, B., 2002. South polar layered deposits of Mars: The cratering record. *Journal of Geophysical Research: Planets*, *107*(E11), pp.10-1.

Lalich, D.E., Holt, J.W. and Smith, I.B., 2019. Radar reflectivity as a proxy for the dust content of individual layers in the Martian north polar layered deposits. *Journal of Geophysical Research: Planets*, *124*(7), pp.1690-1703.

Langevin, Y., Bibring, J.P., Montmessin, F., Forget, F., Vincendon, M., Douté, S., Poulet, F. and Gondet, B., 2007. Observations of the south seasonal cap of Mars during recession in 2004–2006 by the OMEGA visible/near-infrared imaging spectrometer on board Mars Express. *Journal of Geophysical Research: Planets*, *112*(E8).

Laskar, J., Correia, A.C.M., Gastineau, M., Joutel, F., Levrard, B. and Robutel, P., 2004. Long term evolution and chaotic diffusion of the insolation quantities of Mars. *Icarus*, *170*(2), pp.343-364.

Levrard, B., Forget, F., Montmessin, F. and Laskar, J., 2004. Recent ice-rich deposits formed at high latitudes on Mars by sublimation of unstable equatorial ice during low obliquity. *Nature*, *431*(7012), pp.1072-1075.

Levrard, B., Forget, F., Montmessin, F. and Laskar, J., 2007. Recent formation and evolution of northern Martian polar layered deposits as inferred from a Global Climate Model. *Journal of Geophysical Research: Planets*, *112*(E6).

Madeleine, J.B., Forget, F., Head, J.W., Levrard, B., Montmessin, F. and Millour, E., 2009. Amazonian northern mid-latitude glaciation on Mars: A proposed climate scenario. *Icarus*, *203*(2), pp.390-405.

Malin, M.C., Caplinger, M.A. and Davis, S.D., 2001. Observational evidence for an active surface reservoir of solid carbon dioxide on Mars. *Science*, *294*(5549), pp.2146-2148.

Mischna, M.A., Richardson, M.I., Wilson, R.J. and McCleese, D.J., 2003. On the orbital forcing of Martian water and CO2 cycles: A general circulation model study with simplified volatile schemes. *Journal of Geophysical Research: Planets*, *108*(E6).

Montmessin, F., Forget, F., Rannou, P., Cabane, M. and Haberle, R.M., 2004. Origin and role of water ice clouds in the Martian water cycle as inferred from a general circulation model. *Journal of Geophysical Research: Planets*, *109*(E10).

Montmessin, F., Haberle, R.M., Forget, F., Langevin, Y., Clancy, R.T. and Bibring, J.P., 2007. On the origin of perennial water ice at the south pole of Mars: A precession-controlled mechanism?. *Journal of Geophysical Research: Planets*, *112*(E8).

Phillips, R.J., Davis, B.J., Tanaka, K.L., Byrne, S., Mellon, M.T., Putzig, N.E., Haberle, R.M., Kahre, M.A., Campbell, B.A., Carter, L.M. and Smith, I.B.,

2011. Massive CO2 ice deposits sequestered in the south polar layered deposits of Mars. *Science*, *332*(6031), pp.838-841.

Pottier, A., Forget, F., Montmessin, F., Navarro, T., Spiga, A., Millour, E., Szantai, A. and Madeleine, J.B., 2017. Unraveling the Martian water cycle with high-resolution global climate simulations. *Icarus*, *291*, pp.82-106.

Putzig, N.E., Smith, I.B., Perry, M.R., Foss II, F.J., Campbell, B.A., Phillips, R.J. and Seu, R., 2018. Three-dimensional radar imaging of structures and craters in the Martian polar caps. *Icarus*, *308*, pp.138-147.

Richardson, M. I., and R. J. Wilson (2002), Investigation of the nature and stability of the Martian seasonal water cycle with a general circulation model, J. Geophys. Res., 107(E5), 5031, doi:10.1029/2001JE001536.

Seu, R., Phillips, R. J., Biccari, D., Orosei, R., Masdea, A., Picardi, G., et al. (2007). SHARAD sounding radar on the Mars Reconnaissance Orbiter. Journal of Geophysical Research, 112(E5), E05S05. https://doi.org/10.1029/2006JE002745

Smith, I.B., Hayne, P.O., Byrne, S., Becerra, P., Kahre, M., Calvin, W., Hvidberg, C., Milkovich, S., Buhler, P., Landis, M. and Horgan, B., 2020. The Holy Grail: A road map for unlocking the climate record stored within Mars' polar layered deposits. *Planetary and space science*, *184*, p.104841.

Smith, I.B., Schlegel, N.J., Larour, E., Isola, I., Buhler, P.B., Putzig, N.E. and Greve, R., 2022. Carbon dioxide ice glaciers at the south pole of Mars. *Journal of Geophysical Research: Planets*, *127*(4), p.e2022JE007193.

Sori, M.M., Becerra, P., Bapst, J., Byrne, S. and McGlasson, R.A., 2022. Orbital forcing of Martian climate revealed in a south polar outlier ice deposit. *Geophysical Research Letters*, *49*(6), p.e2021GL097450.

Thomas, P.C., Malin, M.C., James, P.B., Cantor, B.A., Williams, R.M.E. and Gierasch, P., 2005. South polar residual cap of Mars: Features, stratigraphy, and changes. *Icarus*, *174*(2), pp.535-559.

Thomas, P.C., Calvin, W., Cantor, B., Haberle, R., James, P.B. and Lee, S.W., 2016. Mass balance of Mars' residual south polar cap from CTX images and other data. *Icarus*, *268*, pp.118-130.

Toon, O. B., Pollack, J. B., Ward, W., Burns, J. A., & Bilski, K. (1980). The astronomical theory of climatic change on Mars. Icarus, 44, 552–607. https://doi.org/10.1016/0019-1035(80)90130-x

Vos, E., Aharonson, O. and Schorghofer, N., 2019. Dynamic and isotopic evolution of ice reservoirs on Mars. *Icarus*, *324*, pp.1-7.

Vos, E., Aharonson, O., Schörghofer, N., Forget, F., Millour, E., Rossi, L., Vals, M. and Montmessin, F., 2022. Stratigraphic and Isotopic Evolution of the Martian Polar Caps From Paleo-Climate Models. *Journal of Geophysical Research: Planets*, *127*(3), p.e2021JE007115.

White, O.L., Moore, J.M., McKinnon, W.B., Spencer, J.R., Howard, A.D., Schenk, P.M., Beyer, R.A., Nimmo, F., Singer, K.N., Umurhan, O.M. and Stern, S.A., 2017. Geological mapping of sputnik planitia on pluto. *Icarus, 287,* pp.261-286.